

# Unlocking air traffic flow prediction through microscopic aircraft-state modeling

Bin Wang<sup>1†</sup>, Anqi Liu<sup>1†</sup>, Jiangtao Zhao<sup>2</sup>, Yanyong Huang<sup>3</sup>,  
Peilan He<sup>1</sup>, Guiyuan Jiang<sup>1</sup>, Feng Hong<sup>1\*</sup>, Yanwei Yu<sup>1\*</sup>,  
Tianrui Li<sup>4</sup>

<sup>1\*</sup>College of Computer Science and Technology, Ocean University of  
China, Qingdao, 266100, Shandong, China.

<sup>2</sup>Sanya Oceanographic Institution, Ocean University of China, Sanya,  
572022, Hainan, China.

<sup>3</sup>Joint Laboratory of Data Science and Business Intelligence,  
Southwestern University of Finance and Economics, Chengdu, 610000,  
Sichuan, China.

<sup>4</sup>School of Computing and Artificial Intelligence, Southwest Jiaotong  
University, Chengdu, 610000, Sichuan, China.

\*Corresponding author(s). E-mail(s): [hongfeng@ouc.edu.cn](mailto:hongfeng@ouc.edu.cn);  
[yuyanwei@ouc.edu.cn](mailto:yuyanwei@ouc.edu.cn);

†These authors contributed equally to this work.

## Abstract

Short-term air traffic flow prediction in terminal airspace is essential for proactive air traffic management. Existing approaches predominantly model traffic flow as aggregated time series, despite traffic dynamics being governed by aircraft states and interactions in continuous airspace. Such aggregation obscures fine-grained information including aircraft kinematics, boundary interactions, and control intent. Here we present AeroSense, a state-to-flow modeling framework that predicts future traffic flow directly from instantaneous airspace situations represented as dynamic sets of aircraft states derived from ADS-B trajectories. By establishing an end-to-end mapping from microscopic aircraft states to future regional traffic flow, AeroSense preserves aircraft-level dynamics while naturally accommodating varying traffic density without relying on historical look-back windows. Experiments on a large-scale real-world dataset show that AeroSense

consistently improves predictive accuracy over aggregation-based forecasting approaches, particularly during high-density traffic periods. These findings suggest that instantaneous airspace situations provide an effective alternative to conventional time-series-based traffic forecasting paradigms.

**Keywords:** Air Traffic Management, Air Traffic Flow Prediction, Flight Trajectory Mining, Spatio-temporal Forecasting, Representation Learning

## 1 Introduction

Air traffic management (ATM) is shifting toward predictive, trajectory-informed operations, where future system states are anticipated rather than reactively controlled (Shi et al. 2021; Guo et al. 2024a). This transition is reflected in major modernization programmes, including the Single European Sky ATM Research (SESAR) initiative in Europe and the Next Generation Air Transportation System (NextGen) in the United States (Brooker 2008), both of which promote the use of trajectory information, such as automatic dependent surveillance-broadcast (ADS-B) data (Zeng et al. 2022), to support coordinated decision-making across the airspace (Nagaoka and Brown 2014). Within this background, understanding the evolution of short-term traffic flow is essential for managing congestion, balancing demand and capacity, and ensuring operational safety (Lin et al. 2019). Accordingly, air traffic flow prediction is not merely a forecasting task, but a core capability for enabling proactive and resilient ATM (Yan et al. 2023; Wandelt et al. 2025). These challenges become especially pronounced in operationally complex airspaces.

Among different airspace types, terminal airspace (TA) is particularly critical (Jurinić et al. 2024; Li et al. 2024; Yin et al. 2025). It serves the interface between en-route airspace and airport surface operations, where arrivals and departures are densely concentrated and frequently subject to air traffic control (ATC) interventions. In such highly dynamic environments, even small fluctuations in traffic conditions can escalate into system-level disruptions (Chen et al. 2016; Jiang and Zhang 2024). The

TA is typically divided into two key functional regions: the Approach Airspace (AP) and the Airspace Control Region (AR)<sup>1</sup>. The AP corresponds to low-altitude airspace near the airport surface and generally exhibits lower traffic volumes, whereas the AR covers higher-altitude airspace with significantly denser flows, as illustrated in Fig. 1. Accurate short-term air traffic flow prediction in both regions is therefore crucial for proactive traffic management (Li et al. 2024), enabling controllers to implement sequencing, holding, and spacing strategies ahead of demand surges (Jurinić et al. 2024).

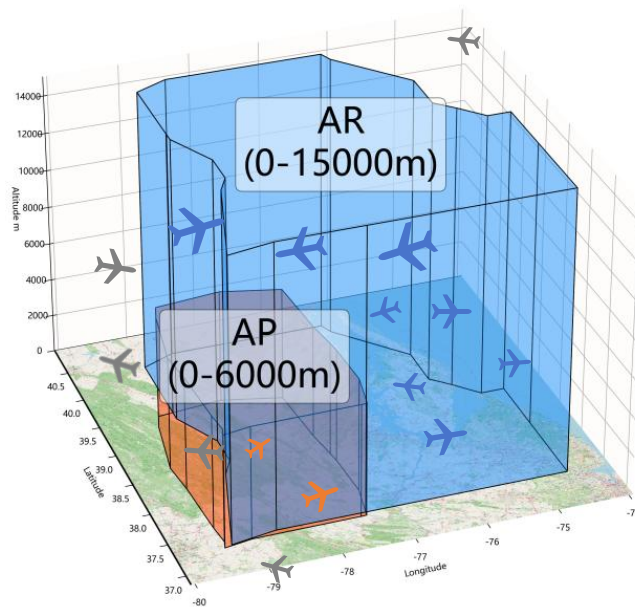


**Fig. 1 Illustration of the AP and AR within TA.** The AP corresponds to low-altitude airspace near the airport surface (typically 0–6000 m), while the AR covers higher-altitude airspace (typically up to 15,000 m) with substantially denser traffic flows. These regions represent the primary focus of ATC operations, whereas traffic outside AP and AR lies beyond direct control.

---

<sup>1</sup>The Airspace Control Region is interchangeably abbreviated as AC. In this study, however, we adopt the abbreviation AR following the terminology accustomed to the local ATC authority.

With the widespread availability of high-resolution ADS-B trajectory data (Strohmeier et al. 2014; Patrikar et al. 2025), data-driven approaches have become the dominant methodology for air traffic flow modeling (Du et al. 2024). Early studies primarily employed statistical learning models, such as support vector machines and gradient boosting trees, to forecast traffic volume from historical observations (Rebollo and Balakrishnan 2014). More recently, deep learning approaches (Yan et al. 2022, 2023), particularly graph neural networks (Zhang et al. 2024) and Transformer-based forecasting models (Ma et al. 2024), have shown strong capability in capturing spatial interactions and temporal dynamics in air traffic flow (Wu et al. 2024).

Despite these advances, existing state-of-the-art (SOTA) approaches largely adhere to a *macroscopic time-series forecasting paradigm*: aircraft trajectories are first aggregated into macroscopic flow sequences or spatio-temporal tensors (Yan et al. 2023; Ma et al. 2024), after which prediction is performed on these derived time-series representations, as illustrated in Fig. 2(b). Such methods primarily rely on statistical correlations learned from aggregated flow sequences, occasionally augmented with temporal embeddings (Zhang et al. 2023). Although operationally convenient, this conventional paradigm largely overlooks the microscopic aircraft-level dynamics. Compressing aircraft states into predefined time-series representations inevitably introduces discretization artifacts, sparsity, and information loss, particularly for fine-grained kinematic cues such as velocity direction and boundary proximity. These observations suggest that the key limitation of existing approaches may not lie in forecasting architectures themselves, but in the underlying representation paradigm used to characterize air traffic dynamics.

We argue that, at any given moment  $t$ , the airspace situation in the TA is more naturally characterized not as a time series, but as a *dynamic, unordered set of aircraft*, whose cardinality continuously changes due to aircraft entry and exit events. This

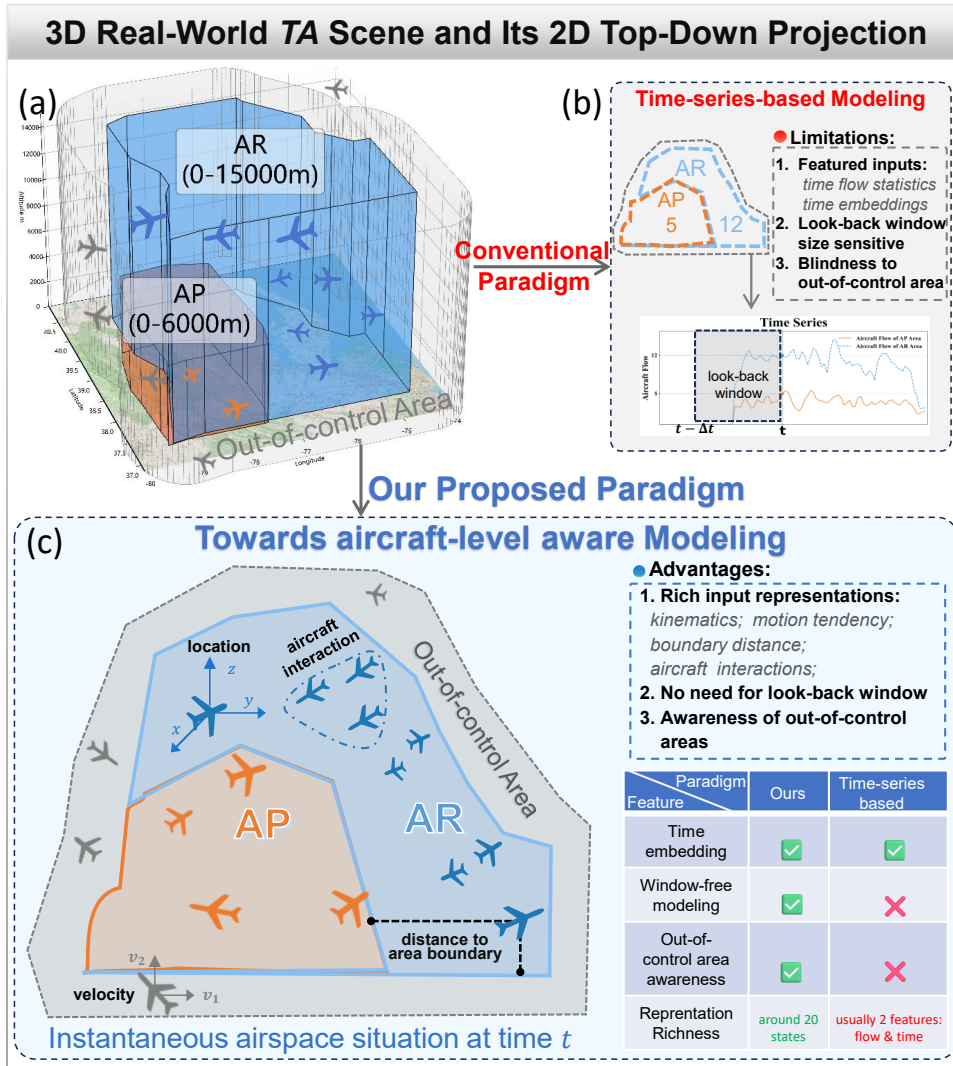


**Fig. 2 The motivation of aircraft-level state modeling.** The proposed aircraft-level modeling paradigm directly models airspace situation for flow prediction of  $(t + \Delta t]$  using only instantaneous aircraft-level states at time  $t$ , without requiring the look-back window.

perspective raises a fundamental requirement: *Can instantaneous microscopic aircraft states provide sufficient information for accurate future air traffic flow prediction without relying on historical flow sequences?*

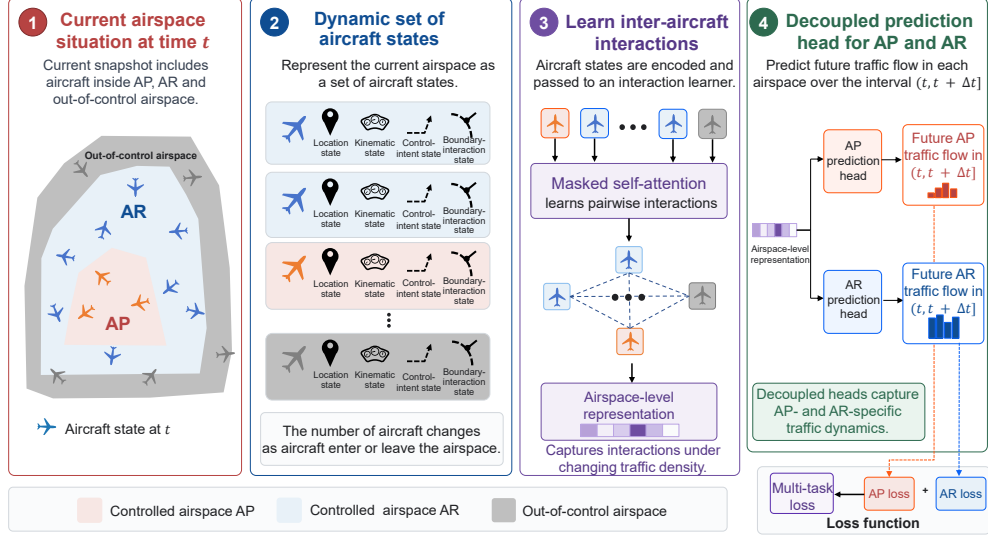


**Fig. 3 Overview of the proposed AeroSense framework.** (1) The instantaneous airspace situation at any time  $t$  is constructed from real-time streaming ADS-B observations without requiring historical trajectory storage or long look-back windows. (2) The current airspace is represented as a dynamic, variable-cardinality set of aircraft states, where each aircraft encodes kinematic information, control intent, boundary interactions, and temporal contextual cues. (3) These aircraft-level states are processed by masked self-attention to capture inter-aircraft interactions under varying traffic density and are subsequently aggregated into an airspace-level representation. (4) Two decoupled prediction heads are employed to separately estimate future traffic flows in the AP and AR regions over the prediction horizon  $(t, t + \Delta t]$ , with both branches jointly optimized during training.

Motivated by this question, we propose *AeroSense*, an *aero* aircraft-level state-to-flow modeling framework that *senses* future traffic flow directly from microscopic aircraft states using ADS-B trajectory data, as illustrated in Fig. 3. Instead of transforming aircraft trajectories into aggregated macroscopic statistics prior to prediction, *AeroSense* formulates the instantaneous airspace situation at time  $t$  as a dynamic, variable-cardinality set of aircraft states and establishes an end-to-end mapping from this set to future airspace-level flows at horizon  $t + \Delta t$ . This formulation preserves fine-grained aircraft kinematics, naturally accommodates varying traffic density, and eliminates the dependence on manually specified *look-back window* hyperparameters that are central to conventional time-series forecasting pipelines. Moreover, because

AeroSense operates directly on instantaneous airspace situations rather than long historical sequences, it is inherently suitable for real-time streaming inference without requiring persistent historical ADS-B trajectory storage.

To realize this formulation, AeroSense incorporates a situation-aware aircraft state representation that encodes physically meaningful cues, including GPS location, boundary interactions, control intent, e.t.c, into the airspace situation modeling process. Building upon these representations, we further develop a permutation-invariant architecture that combines variable-cardinality set handling, masked self-attention for inter-aircraft interaction modeling, and task-decoupled prediction heads to capture the heterogeneous flow dynamics of the AP and AR airspaces.

Our contributions are summarized as follows:

1. We revisit air traffic flow prediction from a macroscopic time-series forecasting problem into a *state-to-flow* learning problem. Instead of relying on aggregated historical flow sequences, we directly model the instantaneous airspace situation as a variable-cardinality set of microscopic aircraft states, thereby aligning the learning representation with the true physical state of air traffic.
2. We propose AeroSense, an aircraft-level state-to-flow modeling framework that establishes an end-to-end mapping from aircraft-level states to future airspace traffic flows. The framework naturally supports dynamic traffic density, eliminates the need for manually specified look-back windows, and mitigates information loss caused by spatio-temporal aggregation.
3. We introduce aircraft-level state representations that encode boundary interactions, control intent, e.t.c, as physically grounded inductive biases. This design enables the model to reason about traffic evolution from underlying flight dynamics rather than relying solely on statistical correlations.

4. Extensive experiments on large-scale real-world terminal airspace data demonstrate that AeroSense consistently outperforms representative SOTA time-series forecasting baselines, particularly under high-density traffic conditions.

## 2 Results

### 2.1 Problem Formulation

**Definition 1** (Airspace Situation) The *Airspace Situation* at instantaneous time  $t$  is formally defined as the set

$$\mathbf{S}_t \stackrel{\text{def}}{=} \{\mathbf{s}_1^{(t)}, \mathbf{s}_2^{(t)}, \dots, \mathbf{s}_{N_t}^{(t)}\}. \quad (1)$$

Each element  $\mathbf{s}_i^{(t)}$ , is extracted from the ADS-B data and represents the state of the  $i$ -th aircraft, which is given by

$$\mathbf{s}_i^{(t)} = [\mathbf{p}_i, \mathbf{v}_i, \phi_i] \in \mathbb{R}^{D_{\text{in}}}, \quad (2)$$

where  $\mathbf{p}_i \in \mathbb{R}^3$  denotes the 3-D aircraft position (longitude, latitude, altitude),  $\mathbf{v}_i \in \mathbb{R}^3$  denotes the 3-D velocity vector,  $\phi_i$  encodes physics-related states such as boundary proximity and flight intention (detailed in Section 4.1). Here,  $D_{\text{in}}$  denotes the total dimensionality of the aircraft-level state as model input vector, and  $N_t = |\mathbf{S}_t|$  represents the number of aircraft present in the airspace at time  $t$ .

*Remark 1* Because aircraft continuously enter and leave the airspace, hence  $N_t$  can vary over time, that is,  $N_t \neq N_{t+1}$  in general. Therefore,  $\mathbf{S}_t$  is inherently a variable-cardinality set, which precludes the direct use of fixed-input-size models such as classical MLPs, CNNs or Transformers.

**Definition 2** (Combined Airspace Scope) Our prediction target focuses on the AR and AP, which together form the *controlled airspace scope*:

$$\Omega_{\text{ctr}} = \text{AP} \cup \text{AR}. \quad (3)$$

The *out-of-control airspace scope*<sup>2</sup> is defined as the surrounding region outside  $\Omega_{\text{ctr}}$  but within a distance threshold  $d$  from its boundary:

$$\Omega_{\text{unctr}} = \left\{ p \in \mathbb{R}^3 \mid 0 < \psi(p; \Omega_{\text{ctr}}) \leq d \right\}. \quad (4)$$

Here,  $\psi(p; \Omega_{\text{ctr}})$  denotes the signed distance from point  $p$  to the boundary of the controlled airspace:

$$\psi(p; \Omega_{\text{ctr}}) = \begin{cases} -\text{dist}(p, \partial\Omega_{\text{ctr}}), & p \in \Omega_{\text{ctr}}, \\ \text{dist}(p, \partial\Omega_{\text{ctr}}), & p \notin \Omega_{\text{ctr}}. \end{cases} \quad (5)$$

where  $p$  denotes a spatial point,  $\partial\Omega_{\text{ctr}}$  denotes the boundary of the controlled airspace, and  $\text{dist}(p, \partial\Omega_{\text{ctr}})$  computes the minimum Euclidean distance from  $p$  to this boundary. The threshold  $d = 100$  km corresponds to the maximum reachable distance within the 15-minute prediction horizon.

The *Combined Airspace Scope* is then formally defined as

$$\Omega \stackrel{\text{def}}{=} \Omega_{\text{ctr}} \cup \Omega_{\text{unctr}}. \quad (6)$$

*Remark 2* Accordingly, the model input in AeroSense is given by  $\mathbf{S}_t = \{\mathbf{s}_i \mid \text{Loc}(\mathbf{s}_i) \in \Omega\}$ , where  $\text{Loc}(\mathbf{s}_i)$  extracts the spatial location of aircraft state  $\mathbf{s}_i$ . This formulation ensures that the model accounts for both aircraft within the controlled airspace  $\Omega_{\text{ctr}}$  and those in the surrounding out-of-control airspace  $\Omega_{\text{unctr}}$ .

**Definition 3** (Prediction Task Modeling) Our objective is to predict the traffic volumes in the airspace of AP and AR, respectively, over a future prediction horizon  $\Delta t$ . The model output is therefore denoted as

$$\hat{\mathbf{Y}}^{(t, \Delta t)} = [\hat{y}_{AP}, \hat{y}_{AR}]^T \in \mathbb{R}^2, \quad (7)$$

where  $\hat{y}_{AP}$  and  $\hat{y}_{AR} \in \mathbb{N}$  denote the predicted traffic volumes within the future interval  $(t, t + \Delta t]$ , in the AP and AR airspaces, respectively. This study focuses on 15-minute-ahead prediction (i.e.,  $\Delta t = 15$  min), which is one of the most operationally relevant short-term

---

<sup>2</sup>See the illustration of the out-of-control airspace in Fig. 2 (a) and (c).

forecasting horizons in ATM. The proposed framework can be naturally extended to longer prediction horizons (e.g.,  $\Delta t = 30$  min or 90 min), as discussed in Section 3.

The *Prediction Task Modeling* is formally defined as constructing a model  $f_\theta : \mathbf{S}_t \rightarrow \mathbb{R}^2$  such that

$$\hat{\mathbf{Y}}^{(t, \Delta t)} \stackrel{\text{def}}{=} f_\theta(\mathbf{S}_t). \quad (8)$$

*Remark 3* The central challenge is to construct a model  $f_\theta$  that can effectively *learn representations from the complex states of all aircraft in the set  $\mathbf{S}_t$ , while simultaneously operating on its variable cardinality.* Since the number of aircraft changes dynamically over time (i.e.,  $N_t \neq N_{t+1}$  in general; see Remark 1), the model must naturally accommodate varying set sizes of  $\mathbf{S}_t$  without relying on fixed-input model structures. This requirement fundamentally challenges conventional architectures such as CNNs, MLPs, and standard Transformers, which typically assume fixed-size inputs.

**Definition 4** (Ground Truth) The ground truth traffic flow  $\mathbf{Y}^{(t, \Delta t)}$  is derived from aircraft trajectories obtained during the target horizon  $(t, t + \Delta t]$ . For a given query time  $t$  and prediction horizon  $\Delta t$ , the *Ground Truth* for the airspace AR and AP is formally defined as

$$y_{AR}^{(t, \Delta t)} \stackrel{\text{def}}{=} |\{i \mid \text{Loc}_\tau(i) \in AR, \exists \tau \in (t, t + \Delta t]\}|, \quad (9)$$

$$y_{AP}^{(t, \Delta t)} \stackrel{\text{def}}{=} |\{i \mid \text{Loc}_\tau(i) \in AP, \exists \tau \in (t, t + \Delta t]\}|. \quad (10)$$

Here,  $\text{Loc}_\tau(i)$  denotes the spatial location of aircraft  $i$  at time  $\tau$ . In other words, each aircraft is counted once if it appears in the target airspace during at any time within  $(t, t + \Delta t]$ . The operator  $|\cdot|$  denotes set cardinality.

## 2.2 Dataset and evaluation metrics

### 2.2.1 Dataset and missing value preprocessing

**Dataset.** A large-scale real-world trajectory dataset was collected from the TA of an international airport, covering the period from March 1 to October 31, 2025. The dataset is derived from operational surveillance records provided by the local ATC authority, where Secondary Surveillance Radar (SSR) and ADS-B measurements are fused into unified aircraft trajectories. The fused trajectory records are sampled at a temporal resolution of 4 seconds.

Each trajectory record contains multi-source aircraft information, including temporal attributes, aircraft identifiers, departure and destination information, spatial positions, kinematic states, control-related variables, and sector-level operational labels. Collectively, these attributes characterize the instantaneous aircraft status from multiple perspectives, including where the aircraft is located, how it is moving, what control intent it may follow, and which operational region it belongs to.

Based on these raw attributes, we further construct aircraft-level state representations that encode location, motion dynamics, control intent, boundary interactions, and temporal context for the subsequent state-to-flow prediction task (detailed in Section 4.1).

**Missing value preprocessing.** Due to occasional missing observations in the original trajectory data, directly sampling aircraft states at an instantaneous timestamp may introduce missing values. To address this issue, we adopt a simple forward-filling strategy. If an aircraft’s state observation is missing at a given timestamp  $t$ , we use its most recent valid state from the preceding timestamps to fill in the missing value. This processing procedure yields a missing-value-free snapshot of the airspace situation. The resulting entire dataset contains 224,904 samples, which are split chronologically into training, validation, and test sets with an 8:1:1 ratio, as summarized in Table 1.

**Table 1** Chronological configuration of the real-world terminal airspace dataset.

Subset	Temporal range	Proportion	Number of samples
Training set	Earliest 80% of the timeline	80%	179,923
Validation set	Subsequent 10% of the timeline	10%	22,490
Test set	Final 10% of the timeline	10%	22,490
Entire dataset	Mar. 1–Oct. 31, 2025	100%	224,904

### 2.2.2 Evaluation metrics

We develop model on the training and validation sets, and evaluate model performance on the test set using MAE, RMSE, and  $R^2$ . Let  $\mathcal{D}_{test} = \{(\mathbf{S}_k^{(t)}, \mathbf{Y}_k^{(t, \Delta t)})\}_{k=1}^N$  denote the test dataset with  $N$  samples, where  $\mathbf{S}_k^{(t)}$  represents the input aircraft states for the  $k$ -th sample, and  $\mathbf{Y}_k^{(t, \Delta t)} = [y_{AP}^k, y_{AR}^k]^\top$  is the ground truth. Let  $\hat{\mathbf{Y}}_k^{(t, \Delta t)} = [\hat{y}_{AP}^k, \hat{y}_{AR}^k]^\top$  denote the corresponding model prediction. Since the prediction results are reported separately for the AP and AR airspaces, the evaluation metrics are computed independently for each airspace  $\mathcal{A}$  as:

$$\text{MAE}_{\mathcal{A}} = \frac{1}{N} \sum_{k=1}^N |\hat{y}_{\mathcal{A}}^k - y_{\mathcal{A}}^k| \quad (11)$$

$$\text{RMSE}_{\mathcal{A}} = \sqrt{\frac{1}{N} \sum_{k=1}^N (\hat{y}_{\mathcal{A}}^k - y_{\mathcal{A}}^k)^2} \quad (12)$$

$$R_{\mathcal{A}}^2 = 1 - \frac{\sum_{k=1}^N (\hat{y}_{\mathcal{A}}^k - y_{\mathcal{A}}^k)^2}{\sum_{k=1}^N (y_{\mathcal{A}}^k - \bar{y}_{\mathcal{A}})^2} \quad (13)$$

where  $\bar{y}_{\mathcal{A}} = \frac{1}{N} \sum_{k=1}^N y_{\mathcal{A}}^k$  denotes the mean ground-truth traffic volume of airspace  $\mathcal{A}$  over the test set.

### 2.3 Comparison baselines

The three baseline groups are designed to isolate different sources of performance gain. 1) Conventional time-series baselines evaluate whether direct microscopic state modeling outperforms classical macroscopic forecasting paradigms. 2) Augmented time-series baselines further test whether the gains can be explained solely by

richer physically grounded inputs. 3) Finally, set-based baselines isolate the effect of permutation-invariant architectures from the proposed aircraft-level state modeling paradigm.

### 2.3.1 Conventional time-series baselines

First, we compare AeroSense against several representative SOTA time-series forecasting models, all of which operate on aggregated historical flow sequences and represent the mainstream macroscopic forecasting paradigm.

- **Autoformer** (Wu et al. 2021): A decomposition-based Transformer that replaces self-attention with an auto-correlation mechanism to capture long-range series-wise dependencies.
- **FEDformer** (Zhou et al. 2022): A frequency-enhanced Transformer that models global temporal patterns through seasonal-trend decomposition in the frequency domain.
- **TimesNet** (Wu et al. 2023): A general-purpose time-series foundation model that transforms one-dimensional sequences into two-dimensional tensors to capture multi-scale temporal variations.
- **iTransformer** (Liu et al. 2024): An inverted Transformer architecture that embeds the entire temporal sequence of each variate to model multivariate correlations.
- **DLinear** (Zeng et al. 2023): A lightweight yet competitive linear forecasting model that decomposes time series into trend and residual components, serving as a strong linear baseline.

*Remark 4* All baselines receive identical input flow sequences covering the previous 24 hours at a 15-minute resolution (i.e., 96 historical time steps), together with temporal embeddings corresponding to the forecast horizon. This setup ensures a fair comparison by providing all baselines with the same historical look-back window and temporal context.

### 2.3.2 Augmented time-series baselines

To examine whether the observed performance gains arise merely from incorporating richer physical information, we further augment the conventional time-series models with physical features derived from aircraft states as below.

For a given target time  $t$ , we first construct a missing-value-free airspace situation following the procedure described in Section 2.2.1. Since time-series models cannot directly process variable-cardinality sets, we aggregate the aircraft states into a fixed-dimensional feature vector. Specifically, the aggregated states include: (i) aircraft counts in the AP, AR, and out-of-control airspace; (ii) summary statistics of boundary proximity to AP and AR, including mean, maximum, and quantiles; (iii) summary statistics of approach factor, including mean values and the proportion of aircraft with positive approach factor; (iv) kinematic statistics such as mean, standard deviation, and maximum ground speed, as well as mean, standard deviation, and absolute-mean vertical speed; (v) inclusion-indicator counts for AP and AR; and (vi) cyclical temporal features.

These aggregated vectors are then stacked into multivariate flow sequences and used as inputs to the augmented time-series models. In this way, the augmented baselines are provided with richer physically grounded states while remaining within the conventional multivariate time-series forecasting framework.

### 2.3.3 Set-based baselines

Finally, we investigate whether the observed performance gains can be attributed solely to the use of permutation-invariant set modeling. To this end, we consider two representative set-based architectures that can directly operate on aircraft-level inputs, enabling a direct comparison that isolates the effect of generic set-based modeling from the proposed airspace-aware design:

- **DeepSets** (Zaheer et al. 2017): The first permutation-invariant model that aggregates independently processed elements via symmetric pooling.
- **SetTransformer** (Lee et al. 2019): An attention-based model designed to capture complex, higher-order interactions among elements.

Both models take the exact same dynamic set of aircraft states as AeroSense as input.

## 2.4 Experimental results and quantitative analysis

To systematically investigate whether microscopic aircraft-state modeling can fundamentally reform air traffic flow prediction, we organize our experiments around three research questions (RQs):

- **RQ1:** Can microscopic aircraft-state modeling fundamentally outperform conventional macroscopic time-series forecasting paradigms?
- **RQ2:** Which microscopic aircraft-state factors and interaction mechanisms contribute most to traffic dynamics?
- **RQ3:** Can the proposed framework maintain robust predictive fidelity under highly dynamic traffic conditions?

### 2.4.1 Validation of the state-to-flow modeling paradigm (RQ1).

**Superior performance over the conventional time-series baselines.** Table 2 reports the quantitative comparison between AeroSense and SOTA time-series forecasting baselines. Overall, time-series models equipped with temporal embeddings consistently outperform their counterparts without such embeddings, highlighting the importance of temporal context. Even under this strengthened setting, AeroSense achieves the best results across all three evaluation metrics, with particularly pronounced gains in the high-volume airspace AR. Among the baselines, TimesNet is the strongest competitor. While compared with TimesNet in the airspace AR, AeroSense reduces MAE by approximately 22.7% (2.100 vs. 2.718) and RMSE by 22.1% (2.806

vs. 3.602), while achieving an  $R^2$  of 0.984. In the airspace AP, AeroSense also attains the lowest error (MAE 1.506) and the highest goodness of fit ( $R^2 = 0.935$ ).

These results demonstrate that microscopic aircraft-level state modeling provides substantially higher predictive accuracy than macroscopic SOTA time-series models, especially for capturing the complex flow dynamics of high-volume airspace AR.

**Table 2** Comprehensive performance comparison with SOTA time-series, augmented, and set-based baselines.

Model	Airspace AP			Airspace AR		
	MAE	RMSE	$R^2$	MAE	RMSE	$R^2$
<i>Conventional time-series baselines</i>						
<i>Autoformer (Wu et al. 2021)</i>						
w/o time embedding	2.048	2.603	0.903	4.238	5.624	0.942
w time embedding	2.052	2.668	0.898	4.361	5.572	0.943
<i>Fedformer (Zhou et al. 2022)</i>						
w/o time embedding	2.153	2.723	0.894	4.247	5.353	0.947
w time embedding	1.872	2.404	0.917	3.170	4.078	0.969
<i>iTransformer (Liu et al. 2024)</i>						
w/o time embedding	2.472	3.232	0.851	4.907	6.269	0.928
w time embedding	1.592	2.083	0.933	3.014	3.835	0.973
<i>DLinear (Zeng et al. 2023)</i>						
w/o time embedding	1.876	2.463	0.913	3.444	4.552	0.962
w time embedding	1.875	2.462	0.913	3.443	4.551	0.962
<i>TimesNet (Wu et al. 2023)</i>						
w/o time embedding	1.765	2.330	0.922	3.330	4.362	0.965
w time embedding	1.545	2.046	0.934	2.718	3.602	0.976
<i>Augmented time-series baselines</i>						
Augmented Autoformer	2.202	2.857	0.865	2.933	3.832	0.969
Augmented Fedformer	2.514	3.319	0.817	3.668	4.742	0.954
Augmented iTransformer	1.863	2.484	0.897	2.568	3.384	0.976
Augmented DLinear	2.001	2.633	0.885	2.481	3.311	0.977
Augmented TimesNet	1.848	2.491	0.897	2.598	3.436	0.975
<i>Set-based baselines</i>						
DeepSets (Zaheer et al. 2017)	<u>1.532</u>	<u>2.096</u>	<u>0.931</u>	<u>2.154</u>	<u>2.861</u>	<u>0.983</u>
SetTransformer (Lee et al. 2019)	1.593	2.206	0.924	2.619	3.553	0.974
<b>AeroSense (Ours)</b>	<b>1.506</b>	<b>2.040</b>	<b>0.935</b>	<b>2.100</b>	<b>2.806</b>	<b>0.984</b>

**Comparison with augmented time-series baselines.** Table 2 also shows that adding aggregated physical-state features to conventional time-series models leads to different effects in the AR and AP airspaces. In the high-volume AR airspace, most augmented variants obtain lower errors than their conventional versions. For example,

the MAE of Autoformer decreases from 4.361 to 2.933 after augmentation, and the MAEs of iTransformer, DLinear, and TimesNet are reduced from 3.014, 3.443, and 2.718 to 2.568, 2.481, and 2.598, respectively. This improvement indicates that the aggregated physical-state features still carry useful information for dense traffic-flow prediction, although they are only coarse summaries of aircraft-level states.

The results in the AP airspace are different. Since AP has a lower traffic volume, its future flow is more sensitive to the states of a small number of individual aircraft. Under this condition, compressing microscopic aircraft states into fixed-dimensional statistics can easily smooth out important aircraft-level differences. As a result, all augmented variants perform worse than their corresponding conventional models in the AP airspace. For instance, the MAE of TimesNet increases from 1.545 to 1.848 after augmentation. Similar degradation is also observed for Autoformer, Fedformer, iTransformer, and DLinear.

These results show that aircraft-state information is useful, especially in dense AR traffic, but the way it is incorporated matters. A coarse aggregation of aircraft states can help conventional time-series models in high-volume airspace, yet it is less reliable in sparse airspace. AeroSense avoids this issue by modeling the aircraft states directly as a variable-cardinality set, which allows the model to preserve aircraft-level information and achieve stable performance in both AP and AR airspaces.

**Comparison with set-based baselines.** The set-based-baseline block of Table 2 shows that directly modeling aircraft states as sets already leads to strong performance. DeepSets achieves MAEs of 1.532 and 2.154 in the AP and AR airspaces, respectively, which are close to the results of AeroSense. SetTransformer also performs better than most conventional time-series baselines, with MAEs of 1.593 in AP and 2.619 in AR. These results indicate that the set-based formulation is well suited to the variable-cardinality nature of airspace situations.

The same block of Table 2 also shows a clear difference between the two generic set-based models. Although SetTransformer introduces an attention mechanism to model interactions among set elements, it does not outperform DeepSets in this task. This difference is more evident in the AR airspace, where the MAE of SetTransformer is 2.619, compared with 2.154 for DeepSets. This suggests that applying a generic set-attention architecture alone is not sufficient for traffic volume prediction. The model also needs to preserve traffic-scale information and adapt the learned representation to the heterogeneous flow patterns of AP and AR.

Compared with these two set-based baselines, AeroSense achieves the lowest errors in both airspaces, with MAEs of 1.506 in AP and 2.100 in AR. The improvement over DeepSets is modest but consistent, while the improvement over SetTransformer is more pronounced, especially in AR. Therefore, the benefit of AeroSense comes not only from adopting a permutation-invariant set representation, but also from its airspace-aware design.

#### 2.4.2 Understanding the role of aircraft-state interactions (RQ2)

To understand the effect of the key design choices in AeroSense, we conduct a comprehensive ablation study. The results are summarized in Table 3.

**Effect of module design.** As shown in Table 3, the *w/o decoupled prediction heads* variant consistently underperforms the full model, increasing the MAE from 1.506 to 1.552 in the AP airspace and from 2.100 to 2.183 in the AR airspace. This result suggests that AP and AR flow prediction require different output mappings due to their distinct traffic densities and aircraft relevance patterns. A shared prediction head couples the two targets and may cause negative transfer when the informative aircraft-state cues differ across airspaces. By using decoupled heads, AeroSense enables airspace-specific prediction branches and reduces interference between the two tasks.

Furthermore, the inclusion of the *masked self-attention* mechanism proves crucial for capturing implicit inter-aircraft dependencies. As indicated in Table 3, removing

**Table 3** Ablation study results of AeroSense. **w/o** denotes the removal of a specific component.

Variant	Airspace AP			Airspace AR		
	MAE	RMSE	R <sup>2</sup>	MAE	RMSE	R <sup>2</sup>
<i>Effect of module design</i>						
w/o Decoupled prediction heads	1.552	2.093	0.932	2.183	2.921	0.983
w/o Masked self-attention	1.567	2.109	0.931	2.149	2.865	0.983
<i>Effect of aircraft-state representation</i>						
w/o State of boundary interactions	1.618	2.175	0.927	2.224	2.977	0.982
w/o State of aircraft location	1.537	2.805	0.933	2.122	2.852	0.983
w/o State of aircraft kinematic	1.543	2.088	0.932	2.231	2.993	0.981
w/o State of temporal context	1.654	2.223	0.923	2.381	3.169	0.979
w/o State of controlling intent	1.578	2.133	0.929	2.132	2.852	0.982
Minimal Physical State	1.672	2.254	0.921	2.317	3.095	0.980
<i>Effect of pooling strategy</i>						
SumPooling→MeanPooling	2.178	2.952	0.865	4.456	6.090	0.924
SumPooling→MaxPooling	2.363	3.178	0.843	5.339	6.899	0.903
<b>AeroSense (Our full model)</b>	<b>1.506</b>	<b>2.040</b>	<b>0.935</b>	<b>2.100</b>	<b>2.806</b>	<b>0.984</b>

this module (*w/o masked self-attention*) leads to a noticeable decline in predictive performance, incurring the MAE from 1.506 to 1.567 in the AP airspace, and from 2.100 to 2.149 in the AR airspace. Without self-attention mechanism, the network processes each aircraft’s state in isolation, thereby failing to capture the structural relationships and interactions among the valid aircrafts. By leveraging masked self-attention, AeroSense dynamically evaluates the relative influence between aircraft pairs, identifying influential aircraft while suppressing irrelevant ones, which is essential for accurately modeling the airspace situation.

**Effect of aircraft-state representation.** As shown in Table 3, removing the boundary interactions states (*w/o State of boundary interactions*) leads to a clear performance drop, with MAE increasing by with the MAE increasing from 1.506 to 1.618 in the AP airspace and from 2.100 to 2.224 in the AR airspace. This decline confirms that merely GPS coordinates alone are insufficient to capture complex boundary dynamics. The conclusion is further supported by the state importance analysis in Fig. 4, where the *approach factor* and *airspace inclusion indicator* rank among the

most influential states. Taken together, these findings suggest that AeroSense relies primarily on relationships between aircraft and airspace, rather than merely memorizing absolute GPS coordinates.

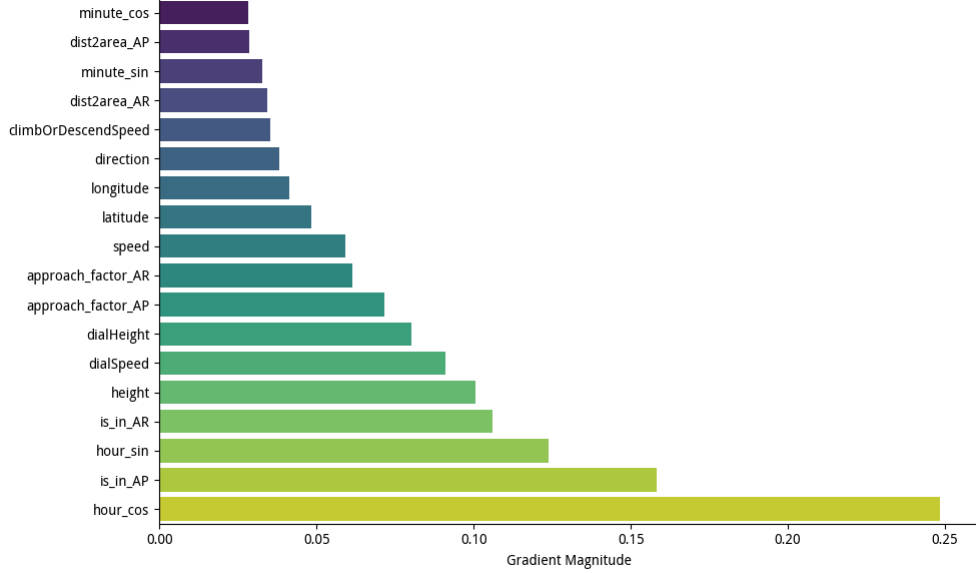


**Fig. 4 Importance of the proposed aircraft states.** The y-axis lists the proposed microscopic aircraft states. The x-axis represents the gradient magnitude, which measures the sensitivity of the model prediction to each state.

To further examine whether the necessity of the designed physics-informed states, we evaluate a *Minimal Physical State* variant that retains only basic location and kinematic states. As reported in Table 3, this simplified variant still achieves competitive performance (AP MAE 1.672, AR MAE 2.317), remaining substantially stronger than conventional time-series baselines in both the AR and AP airspaces. This finding suggests that the primary performance gain originates from the proposed state-to-flow modeling paradigm itself, while the full situation-aware state representation provides additional performance improvements.

**Effect of pooling strategy.** The choice of pooling strategy is a fundamental structural design in AeroSense rather than a simple implementation detail. As shown

in Table 3, replacing the default *SumPooling* operator (defined in Eq. (29)) with alternative aggregation strategies leads to substantial performance degradation. In the high-density AR airspace, adopting *MeanPooling* and *MaxPooling* increases the MAE from 2.100 to 4.456 and 5.339, respectively. Similar trends are also observed in the AP airspace.

*Why is the pooling strategy so influential?* The key reason lies in the intrinsic nature of air traffic flow prediction. Traffic volume is fundamentally an accumulative quantity over aircraft: it depends on the number of relevant aircraft and their individual contributions to future flow, rather than on the averaged state of a typical aircraft or the response of a single dominant aircraft. Consequently, the global airspace representation should remain sensitive to the number of valid aircraft contained in the input set.

Consider two traffic situations with similar average aircraft states but substantially different aircraft counts. Under *MeanPooling*, these situations may produce nearly identical global representations despite corresponding to very different future traffic volumes. In contrast, *MaxPooling* introduces another limitation by preserving only the strongest activation along each feature dimension while discarding contributions from the remaining aircraft. Such behavior is also unsuitable for flow prediction, where multiple moderately relevant aircraft may jointly determine future traffic demand.

By comparison, *SumPooling* accumulates the representations of all valid aircraft and therefore better aligns with the counting nature of the prediction task. Under this formulation, each aircraft can be interpreted as contributing a certain amount of evidence toward future AP or AR traffic flow. By simultaneously preserving aircraft-level state information and the scale of the aircraft set, *SumPooling* provides a more appropriate global representation for air traffic flow prediction.

### 2.4.3 Robustness under temporally heterogeneous traffic conditions (RQ3)

Air traffic flows exhibit pronounced temporal heterogeneity, with substantial demand surges during morning and evening peak periods. To systematically evaluate the robustness of AeroSense under such volatile conditions, we conduct a dayparting multi-object evaluation by analyzing the prediction errors across different time periods over a full 24-hour cycle. Specifically, the day is partitioned into twelve non-overlapping 2-hour intervals, each treated as an independent evaluation objective.

As shown in Fig. 5, AeroSense consistently achieves low MAE across all time intervals in both the AP and AR airspaces. In particular, *AeroSense attains Pareto-optimal performance in the AR airspace*, forming a dominant error frontier that is not surpassed by any baseline under this dayparting multi-objective evaluation. The advantage of AeroSense is especially pronounced during high-volatility periods, such as the morning congestion peak (08:00–10:00). Whereas macroscopic time-series baselines (e.g., Autoformer and FEDformer) exhibit substantial degradation with sharp error spikes. For instance, their MAE surge to approximately 4.2 and 3.5 in the AR airspace during this morning peak. AeroSense maintains a smoother and more stable error profile, keeping its MAE at a significantly lower level of roughly 2.8. A similar contrast is observed during the late-night period (22:00–24:00); while the Autoformer error spikes dramatically to nearly 7.0 in the AR and 2.9 in the AP, AeroSense remains highly robust, with its MAE dropping below 2.0 and 1.5, respectively. This robustness demonstrates that directly modeling instantaneous aircraft states allows the model to rapidly adapt to highly dynamic traffic flow transitions, providing more reliable predictions during sudden demand surges.

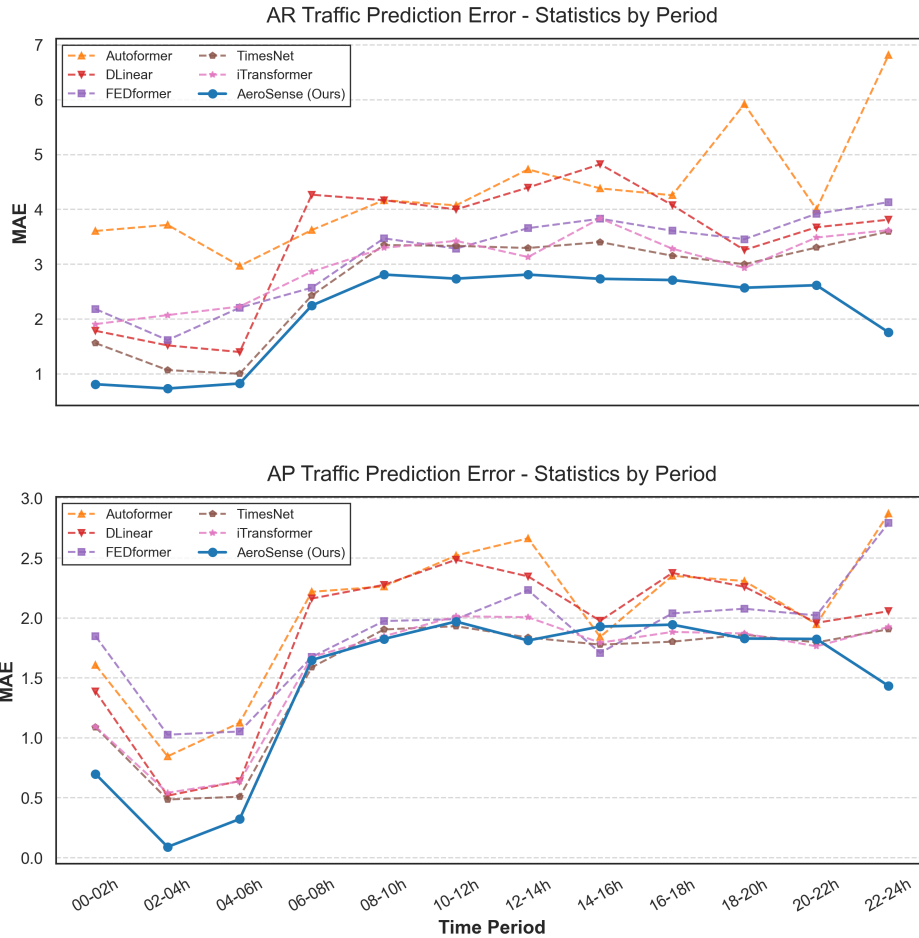


**Fig. 5 Prediction errors across different time periods for dayparting multi-object evaluation.** The figure presents the MAE statistics of different models over a 24-hour cycle under dayparting multi-object evaluation for the AR (top) and AP (bottom) airspaces. Each point corresponds to the average prediction error within a two-hour interval. Compared with conventional time-series baselines, AeroSense maintains consistently lower prediction errors across most time periods, particularly during high-traffic daytime intervals characterized by stronger traffic fluctuations and operational complexity.

## 2.5 Case study

Finally, we provide qualitative visualizations to illustrate how AeroSense assigns task-conditioned relevance under two target airspaces.

### 2.5.1 Visualization of task-specific attention weights

Fig. 6 visualizes instance-level influence scores for the same traffic situation under AR and AP flow prediction tasks, showing how AeroSense adaptively attends to aircraft states in a task-conditioned manner. A clear contrast is observed for the aircraft marked by *Arrow 2*. In the AR prediction task (Scenario a), the model assigns this aircraft a high attention weight, identifying it as a key contributor to AR flow. In contrast, in the AP prediction task (Scenario b), the attention weight assigned to the same aircraft is substantially reduced because its kinematic trend does not indicate convergence toward the AP airspace. By comparison, the aircraft marked by *Arrow 1*, which is located in the out-of-control airspace, consistently receives low attention in both scenarios. This indicates that the model correctly treats it as background traffic that is irrelevant to flow prediction in either airspace.

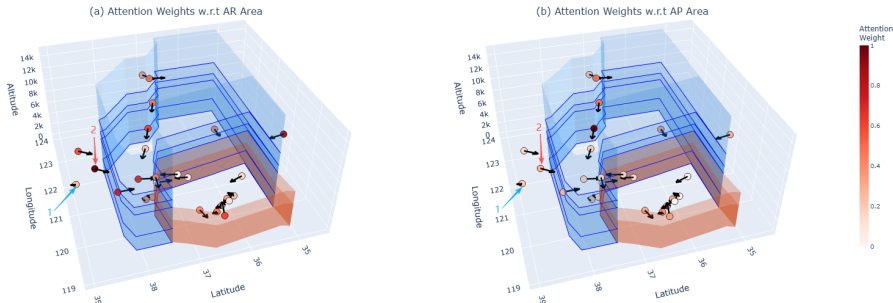


**Fig. 6 Visualization of aircraft-state representation.** Spatial attention weights for the same traffic situation at time  $t$  under (a) AR and (b) AP flow prediction tasks (darker colors indicate higher importance). The aircraft marked by *Arrow 2* receives high attention for AR prediction but is suppressed for AP prediction, reflecting task-specific adaptation. In contrast, the aircraft marked by *Arrow 1* remains consistently down-weighted in both cases, indicating effective noise suppression. These patterns demonstrate that AeroSense dynamically decouples traffic relevance based on task-dependent kinematic constraints.

### 2.5.2 Visualization of inter-aircraft interaction

Fig. 7 visualizes the self-attention weights learned by AeroSense to illustrate how inter-aircraft interactions are modeled. The heatmap presents normalized Softmax attention

scores, where the  $x$ -axis denotes source aircraft and the  $y$ -axis denotes receiver aircraft, thereby indicating the relative influence between aircraft pairs. The resulting attention patterns are neither uniform nor symmetric. Instead, the model selectively assigns higher attention to a subset of aircraft. This behavior suggests that AeroSense can identify influential aircraft while suppressing irrelevant ones, yielding interaction patterns that are broadly consistent with realistic air traffic dynamics.

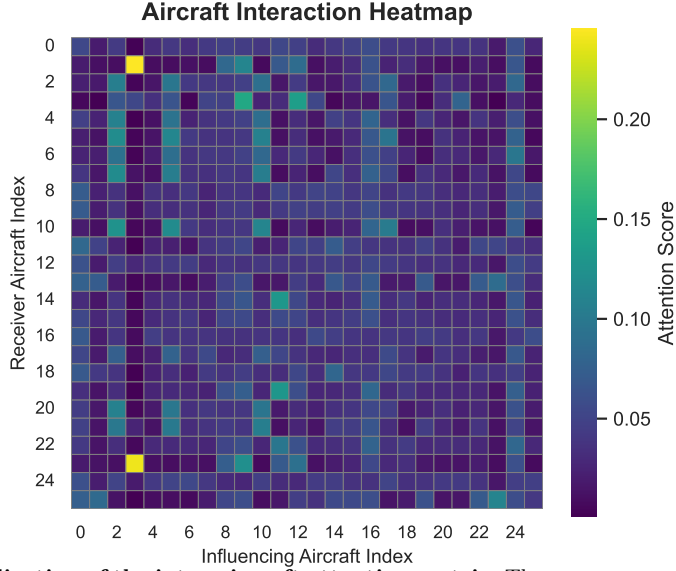


**Fig. 7 Visualization of the inter-aircraft attention matrix.** The axes correspond to the aircraft indices within the input set. The heatmap depicts the attention weights, indicating the potential influence of the source aircraft ( $x$ -axis) on the receiver aircraft ( $y$ -axis).

### 3 Discussion

**Conclusions.** This paper revisits air traffic flow prediction from a fundamentally different perspective. We argue that the conventional macroscopic paradigm, which relies on aggregated time-series observations, introduces an inherent mismatch between the learning representation and the true physical state of air traffic. In practice, traffic in the TA is more naturally characterized as a dynamic, variable-cardinality set of aircraft evolving in continuous airspace. To address this mismatch, we propose

*AeroSense*, a state-to-flow modeling framework that directly maps microscopic aircraft states to macroscopic traffic flows. By explicitly representing the instantaneous airspace situation as a dynamic set, AeroSense removes the need for historical look-back windows and mitigates the information loss caused by spatial and temporal aggregation. Extensive experiments on a large-scale real-world TA dataset demonstrate that AeroSense consistently outperforms strong time-series baselines. The results show that directly modeling microscopic aircraft states leads to substantially higher predictive fidelity. Beyond improving average predictive accuracy, AeroSense also exhibits strong robustness during peak periods and nearly achieves Pareto-optimal performance under dayparting multi-objective evaluation, underscoring its practical value for proactive ATM.

From a deployment perspective, this design also simplifies real-time streaming inference. Because AeroSense does not require long historical windows of aggregated traffic statistics for online prediction, it can reduce storage overhead and simplify variable maintenance in streaming systems, e.g., Kafka. This property also aligns with recent efforts toward lightweight and deployable 4D trajectory prediction for real-time ATM applications (Tang et al. 2025).

**Limitations and future works.** This study primarily focuses on short-term 15-minute-ahead forecasting, as this horizon is among the most operationally relevant for ATC authorities. Accordingly, AeroSense is currently deployed for short-term traffic prediction in practice. Extending the framework to longer forecasting horizons, such as 30-minute-ahead and 90-minute-ahead prediction tasks (Zhang et al. 2024), is both natural and an important direction for future research. In addition, the current framework mainly models aircraft-state-driven traffic dynamics. Future work may further incorporate external factors, including weather conditions (Zeng et al. 2024) and richer spoken instructions (Guo et al. 2024b), to further enhance predictive performance under rapidly evolving traffic situations.

## 4 Methods

### 4.1 Aircraft-level state representation

We next construct an aircraft-state representation from trajectory data to encode aircraft kinematics, pilot control intent, boundary interactions, and temporal context. Each aircraft at time  $t$  is represented by a state vector  $\mathbf{s}_i^{(t)} \in \mathbb{R}^{D_{\text{in}}}$ , where  $D_{\text{in}} = 18$  in this study. The state vector is formed by concatenating the following five groups of states derived from raw ADS-B data:

**1. State of aircraft location  $\mathbf{f}_l$ .** The location state describes the aircraft position, including latitude  $\varphi$ , longitude  $\lambda$ , and barometric altitude  $H$ :

$$\mathbf{f}_l = [\varphi, \lambda, H] \in \mathbb{R}^3. \quad (14)$$

**2. State of aircraft kinematic  $\mathbf{f}_k$ .** The kinematic state captures instantaneous motion using ground speed  $v_{gs}$ , vertical speed  $v_{vs}$ , and heading angle  $\theta$ :

$$\mathbf{f}_k = [v_{gs}, v_{vs}, \theta] \in \mathbb{R}^3. \quad (15)$$

**3. State of controlling intent  $\mathbf{f}_c$ .** To reflect controller or pilot intention, we incorporate intention-driven settings from *Mode Control Panel*, including dialed airspeed  $v_{dial}$  and dialed altitude  $h_{dial}$ :

$$\mathbf{f}_c = [v_{dial}, h_{dial}] \in \mathbb{R}^2. \quad (16)$$

**4. State of boundary interactions  $\mathbf{f}_b$ .** To explicitly encode how an aircraft relates to the surrounding airspace geometry, we introduce boundary-interaction state that describe both its spatial position relative to a target airspace and its motion trend with respect to that airspace. Two quantities are defined.

1) *State of boundary proximity*  $d_{\mathcal{A}}$ : To capture geometric effects associated with airspace entry and exit, we compute the minimum distance from the aircraft location  $\mathbf{p}_i$  to the boundary  $\partial\Omega_{\text{ctr}}$  of airspace  $\mathcal{A}$ , i.e., AR or AP:

$$d_{\mathcal{A}} = \min_{\mathbf{b} \in \mathcal{A}} \text{dist}(p_i, b). \quad (17)$$

This quantity reflects how close the aircraft is to the corresponding airspace boundary and therefore provides a direct cue about potential near-term transitions across airspaces.

2) *Approach factor*  $\alpha_{\mathcal{A}}$ : To distinguish approaching traffic from bypassing or departing traffic, we further characterize the aircraft motion trend relative to the airspace center  $\mathbf{c}_{\mathcal{A}}$ . Let  $\mathbf{r}_c = \mathbf{c}_{\mathcal{A}} - \mathbf{p}_i$  denote the relative position vector from the aircraft to the airspace center. The approach factor is defined as the cosine similarity between the velocity vector  $\mathbf{v}_i$  and  $\mathbf{r}_c$ :

$$\alpha_{\mathcal{A}} = \frac{\mathbf{v}_i \cdot \mathbf{r}_c}{\|\mathbf{v}_i\|_2 \|\mathbf{r}_c\|_2 + \epsilon} \quad (18)$$

Here,  $\alpha_{\mathcal{A}} > 0$  indicates motion toward the airspace center, whereas  $\alpha_{\mathcal{A}} < 0$  indicates motion away from it.

We compute these states for both AP and AR, yielding:

$$\mathbf{f}_b = [d_{AP}, d_{AR}, \alpha_{AP}, \alpha_{AR}, I_{AP}, I_{AR}] \in \mathbb{R}^6, \quad (19)$$

where  $I_{\mathcal{A}} \in \{0, 1\}$  denotes the airspace inclusion indicator for aircraft  $i$ , with  $I_{\mathcal{A}} = 1$  if the aircraft is currently located within airspace  $\mathcal{A}$  and 0 otherwise. Together, these states provide complementary geometric and kinematic cues for describing how aircraft interact with the AP and AR boundaries.

**5. State of temporal context  $\mathbf{f}_t$ .** Temporal context is encoded using cyclical embeddings to capture recurring temporal patterns in air traffic, such as intraday and

intra-hour variability. Given the timestamp at time  $t$ , we extract the hour  $h_t \in [0, 24)$  and minute  $m_t \in [0, 60)$ . The temporal feature vector is then defined as

$$\mathbf{f}_t = \left[ \sin\left(\frac{2\pi h_t}{24}\right), \cos\left(\frac{2\pi h_t}{24}\right), \sin\left(\frac{2\pi m_t}{60}\right), \cos\left(\frac{2\pi m_t}{60}\right) \right] \in \mathbb{R}^4 \quad (20)$$

where the periods 24 and 60 correspond to the cycles used to normalize the hour and minute components, respectively.

The final aircraft state is constructed via concatenation ( $\oplus$ ) as

$$\mathbf{s}_i^{(t)} = \text{Norm}(\mathbf{f}_l \oplus \mathbf{f}_k \oplus \mathbf{f}_c) \oplus \mathbf{f}_b \oplus \mathbf{f}_t \in \mathbb{R}^{18} \quad (21)$$

where  $\text{Norm}(\cdot)$  applies z-score normalization to  $\mathbf{f}_l$ ,  $\mathbf{f}_k$ , and  $\mathbf{f}_c$ , while  $\mathbf{f}_b$  and  $\mathbf{f}_t$  are left unnormalized.

## 4.2 Model architecture of AeroSense

This subsection presents the AeroSense architecture, with particular emphasis on variable-cardinality set handling, inter-aircraft interaction modeling, and task-specific prediction.

### 4.2.1 Variable-cardinality set handling via container initialization

The input to AeroSense is the aircraft state set  $\mathbf{S}_t$  defined in Section 4.1. For each time step  $t$ , the set is arranged into a matrix container  $\mathbf{X} \in \mathbb{R}^{N_{max} \times D_{in}}$ :

$$\mathbf{X} = [\mathbf{s}_1, \dots, \mathbf{s}_{N_t}, \mathbf{s}_{1+N_t}, \dots, \mathbf{s}_{N_{max}}]^\top \quad (22)$$

where  $\mathbf{s}_1, \dots, \mathbf{s}_{N_t}$  correspond to the valid states in  $S_t$ , and  $\mathbf{s}_{1+N_t}, \dots, \mathbf{s}_{N_{max}}$  are zero-padding vectors. Here,  $N_{max}$  denotes a predefined upper bound on the set cardinality. Exploratory data analysis shows that the maximum number of aircraft simultaneously

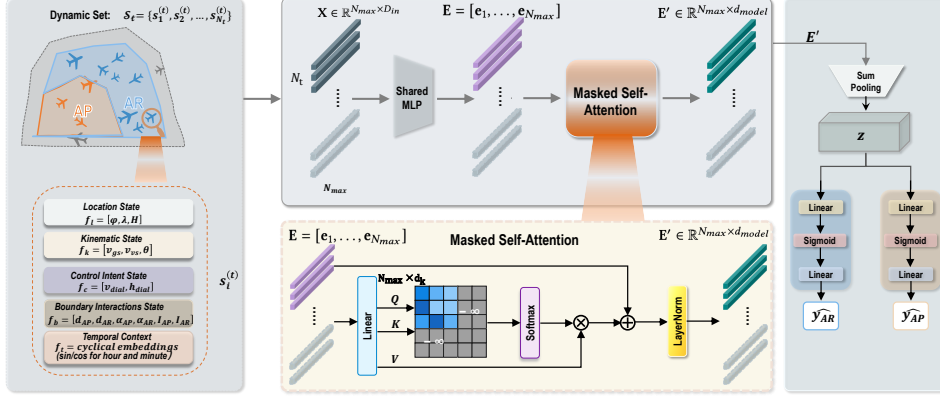


**Fig. 8 The architecture of the proposed AeroSense model.** This figure illustrates the key variables and computational steps of the inference pipeline, corresponding to Equations 14–30. The instantaneous airspace situation at time  $t$  is represented as a dynamic set of aircraft states  $\mathbf{S}_t = \{\mathbf{s}_1^{(t)}, \mathbf{s}_2^{(t)}, \dots, \mathbf{s}_{N_t}^{(t)}\}$ , where each state encodes aircraft location, kinematics, control intent, boundary interactions, and temporal context. The variable-cardinality aircraft set is formatted into a fixed-capacity container and encoded through a shared MLP, followed by masked self-attention to model inter-aircraft interactions while filtering padded states. The resulting aircraft representations are aggregated via *SumPooling* to produce a global airspace-level representation, which is then fed into two decoupled prediction branches for future AP and AR traffic flow prediction.

present across the out-of-control airspace, AR, and AP is 105, while more than 99% of time steps contain fewer than 80 aircraft. Accordingly, we set the maximum input cardinality to  $N_{max} = 120$  to cover all traffic scenarios, including peak periods.

#### 4.2.2 Deep representation learning from input state

Given the matrix  $\mathbf{X}$ , each row  $\mathbf{s}_i \in \mathbb{R}^{D_{in}}$  for  $i = 1, \dots, N_{max}$  represents the state of one aircraft. To learn expressive aircraft-level representations, we use a weight-shared MLP to project these physical states into a latent space. Let  $\mathbf{h}_i^{(0)} = \mathbf{s}_i$  denote the input to the first layer. The propagation at the  $l$ -th layer is defined as

$$\mathbf{h}_i^{(l)} = \text{Dropout} \left( \text{ReLU} \left( \text{BN} \left( \mathbf{W}^{(l)} \mathbf{h}_i^{(l-1)} + \mathbf{b}^{(l)} \right) \right) \right) \quad (23)$$

where  $\mathbf{W}^{(l)}$  and  $\mathbf{b}^{(l)}$  are the learnable parameters of the  $l$ -th layer. Here,  $\text{BN}(\cdot)$  and  $\text{Dropout}(\cdot)$  denote batch normalization (Ioffe and Szegedy 2015) and dropout regularization (Srivastava et al. 2014), respectively, and  $\text{ReLU}(\cdot)$  denotes the rectified linear unit activation function. The resulting aircraft embedding is denoted by

$$\mathbf{e}_i = \mathbf{h}_i^{(L)} \in \mathbb{R}^{d_{model}}, \quad (24)$$

where  $d_{model}$  is the latent space dimension.

### 4.2.3 Aircraft interaction modeling via self-attention

To capture implicit inter-aircraft dependencies and global correlations within the traffic scene, we employ a multi-head self-attention mechanism (Vaswani et al. 2017). As introduced earlier, because neural networks require fixed-size inputs, the variable-length set of aircraft is padded to a maximum capacity  $N_{max}$ . Within this sequence, only the first  $N_t$  elements correspond to *valid aircraft states*—meaning the actual aircraft physically present in the modeled airspace at time  $t$ —while the remaining  $N_{max} - N_t$  elements are zero-padded dummy states.

To prevent these artificial padding states from interfering with the interaction modeling, we introduce an attention masking mechanism. The goal of the mask is to ensure that the self-attention operation exclusively considers the valid aircraft. We define a mask matrix  $M \in \mathbb{R}^{N_{max} \times N_{max}}$  as follows:

$$M_{ij} = \begin{cases} 0, & \text{if } 1 \leq i \leq N_t \text{ and } 1 \leq j \leq N_t \\ -\infty, & \text{otherwise} \end{cases} \quad (25)$$

Let  $\mathbf{E} = [\mathbf{e}_1, \dots, \mathbf{e}_{N_{max}}]^\top$  denote the matrix of aircraft embeddings. For the  $j$ -th attention head, the query ( $\mathbf{Q}_j$ ), key ( $\mathbf{K}_j$ ), and value ( $\mathbf{V}_j$ ) matrices are computed via

linear projections:

$$\mathbf{Q}_j = \mathbf{E}\mathbf{W}_Q^j, \quad \mathbf{K}_j = \mathbf{E}\mathbf{W}_K^j, \quad \mathbf{V}_j = \mathbf{E}\mathbf{W}_V^j. \quad (26)$$

Then, the scaled dot-product  $\mathbf{Q}_j\mathbf{K}_j^\top$  computes the pairwise similarity as the interaction strength between different aircraft. The mask matrix  $M$  is then added to this result before applying the Softmax function to obtain the normalized attention weights:

$$\mathbf{A}_j = \text{Softmax} \left( \frac{\mathbf{Q}_j\mathbf{K}_j^\top}{\sqrt{d_k}} + M \right) \mathbf{V}_j \quad (27)$$

By assigning  $-\infty$  to the padding positions in  $M$ , their corresponding attention weights are strictly driven to 0 after the Softmax operation. Consequently, the padded items are completely filtered out, allowing the model to focus solely on the structural relationships and interactions among the truly valid aircraft.

#### 4.2.4 Padding state filtering and summation pooling

We next employ a permutation-invariant aggregation function  $\rho$  to obtain a fixed-length global context vector  $\mathbf{z}$ . Unlike classification tasks, where Max or Mean pooling is often sufficient, traffic flow prediction is fundamentally a volume regression problem that depends on the number of aircraft in the set. Motivated by deep sets theory (Zaheer et al. 2017), we therefore instantiate  $\rho$  as element-wise summation (hereafter referred to as *SumPooling*), which preserves traffic scale in the global representation. Because the matrix container  $\mathbf{X}$  is padded to length  $N_{max}$ , we introduce an indicator function  $\mathbb{I}_{filter}(i)$  to remove padding states during aggregation:

$$\mathbb{I}_{filter}(i) = \begin{cases} 1 & \text{if } 1 \leq i \leq N_t \\ 0 & \text{otherwise} \end{cases} \quad (28)$$

We formalize this *SumPooling* operation to compute the global representation  $\mathbf{z}$  as follows:

$$\mathbf{z} = \rho(\{\mathbf{e}'_1, \dots, \mathbf{e}'_{N_{max}}\}) = \sum_{i=1}^{N_{max}} \mathbf{e}'_i \cdot \mathbb{I}_{filter}(i) \quad (29)$$

By explicitly summing the valid states, this *SumPooling* captures total traffic accumulation, ensuring that the model remains sensitive to aircraft count rather than only to average state characteristics.

#### 4.2.5 Prediction via decoupled heads

Because the AP and AR exhibit distinct traffic patterns and flow distributions, we design two independent decoder prediction heads  $g_{\mathcal{A}}(\cdot)$ , one for each airspace. The global context vector  $\mathbf{z}$  is fed into both branches:

$$\hat{y}_{\mathcal{A}} = g_{\mathcal{A}}(\mathbf{z}) = \mathbf{W}_{\mathcal{A}}^{(2)} \text{ReLU} \left( \mathbf{W}_{\mathcal{A}}^{(1)} \mathbf{z} + \mathbf{b}_{\mathcal{A}}^{(1)} \right) + b_{\mathcal{A}}^{(2)} \quad (30)$$

where  $\mathbf{W}_{\mathcal{A}}^{(l)}$  and  $\mathbf{b}_{\mathcal{A}}^{(l)}$  denote the learnable weight matrix and bias vector of the  $l$ -th layer for airspace  $\mathcal{A}$ . The final model output is  $\hat{\mathbf{Y}} = [\hat{y}_{AP}, \hat{y}_{AR}]^{\top}$ .

### 4.3 Multi-task loss function

We adopt the Huber loss as the training objective. This loss combines the smooth optimization behavior of MSE for small errors with the robustness of MAE to large deviations. The total loss is defined as the sum of prediction errors over both target airspaces:

$$\mathcal{L}(\Theta) = \frac{1}{B} \sum_{k=1}^B \sum_{\mathcal{A} \in \{AP, AR\}} \mathcal{L}_{\delta}(y_{\mathcal{A}}^{(k)} - \hat{y}_{\mathcal{A}}^{(k)}) \quad (31)$$

where  $B$  denotes the batch size. The Huber loss is defined as follows, with  $\delta = 1.0$  in our experiments and  $a = y - \hat{y}$  denoting the prediction residual:

$$\mathcal{L}_\delta(a) = \begin{cases} \frac{1}{2}a^2 & \text{if } |a| \leq \delta, \\ \delta(|a| - \frac{1}{2}\delta) & \text{otherwise.} \end{cases} \quad (32)$$

## 5 Data availability

Source data are provided with this paper.

## 6 Code availability

The source code is publicly available at [https://github.com/aspjy/aerosense\\_open](https://github.com/aspjy/aerosense_open).

## References

- Brooker P (2008) SESAR and nextgen: Investing in new paradigms. *Journal of Navigation* 61(2):195–208
- Chen D, Hu M, Ma Y, et al (2016) A network-based dynamic air traffic flow model for short-term en route traffic prediction. *Journal of Advanced Transportation* 50(8):2174–2192
- Du W, Chen S, Li Z, et al (2024) A spatial-temporal approach for multi-airport traffic flow prediction through causality graphs. *IEEE Transactions on Intelligent Transportation Systems* 25(1):532–544
- Guo D, Zhang Z, Yan Z, et al (2024a) FlightBERT++: A non-autoregressive multi-horizon flight trajectory prediction framework. *Proceedings of the AAAI Conference on Artificial Intelligence* 38(1):127–134
- Guo D, Zhang Z, Yang B, et al (2024b) Integrating spoken instructions into flight trajectory prediction to optimize automation in air traffic control. *Nature Communications* 15(1):9662

- Ioffe S, Szegedy C (2015) Batch normalization: Accelerating deep network training by reducing internal covariate shift. In: International Conference on Machine Learning (ICML), pp 448–456
- Jiang F, Zhang Z (2024) Characteristics of air traffic flow in terminal airspace: A multiplex recurrence network analysis. *IEEE Transactions on Intelligent Transportation Systems* 25(10):14803–14815
- Jurinić T, Juričić B, Antulov-Fantulin B, et al (2024) Defining terminal airspace air traffic complexity indicators based on air traffic controller tasks. *Aerospace* 11(5)
- Lee J, Lee Y, Kim J, et al (2019) Set transformer: A framework for attention-based permutation-invariant neural networks. In: International Conference on Machine Learning (ICML), pp 3744–3753
- Li Y, Jiang B, Liu W, et al (2024) Airspace situation analysis of terminal area traffic flow prediction based on big data and machine learning methods. *Big Data Research* 35:100425
- Lin Y, Zhang Jw, Liu H (2019) Deep learning based short-term air traffic flow prediction considering temporal–spatial correlation. *Aerospace Science and Technology* 93:105113
- Liu Y, Hu T, Zhang H, et al (2024) iTransformer: Inverted transformers are effective for time series forecasting. In: International Conference on Learning Representations (ICLR)
- Ma C, Alam S, Cai Q, et al (2024) Text-Enriched air traffic flow modeling and prediction using transformers. *IEEE Transactions on Intelligent Transportation Systems* 25(7):7963–7976

- Nagaoka S, Brown M (2014) A review of safety indices for trajectory-based operations in air traffic management. *Transactions of the Japan Society for Aeronautical and Space Sciences, Aerospace Technology Japan* 12(APISAT-2013):a43–a49
- Patrikar J, Dantas J, Moon B, et al (2025) Image, speech, and ADS-B trajectory datasets for terminal airspace operations. *Scientific Data* 12(1):468
- Rebollo JJ, Balakrishnan H (2014) Characterization and prediction of air traffic delays. *Transportation Research Part C: Emerging Technologies* 44:231–241
- Shi Z, Xu M, Pan Q (2021) 4-D flight trajectory prediction with constrained lstm network. *IEEE Transactions on Intelligent Transportation Systems* 22(11):7242–7255
- Srivastava N, Hinton G, Krizhevsky A, et al (2014) Dropout: a simple way to prevent neural networks from overfitting. *The Journal of Machine Learning Research* 15(1):1929–1958
- Strohmeier M, Schäfer M, Lenders V, et al (2014) Realities and challenges of nextgen air traffic management: the case of ADS-B. *IEEE Communications Magazine* 52(5):111–118
- Tang W, Dai J, Huang Z, et al (2025) 4D trajectory lightweight prediction algorithm based on knowledge distillation technique. *Frontiers in Neurorobotics* 19:1643919
- Vaswani A, Shazeer N, Parmar N, et al (2017) Attention is all you need. In: *Advances in Neural Information Processing Systems (NeurIPS)*
- Wandelt S, Chen X, Sun X (2025) Flight delay prediction: A dissecting review of recent studies using machine learning. *IEEE Transactions on Intelligent Transportation Systems* 26(4):4283–4297

- Wu H, Xu J, Wang J, et al (2021) Autoformer: Decomposition transformers with auto-correlation for long-term series forecasting. In: Advances in Neural Information Processing Systems (NeurIPS), pp 22419–22430
- Wu H, Hu T, Liu Y, et al (2023) TimesNet: Temporal 2D-variation modeling for general time series analysis. In: International Conference on Learning Representations (ICLR)
- Wu Y, Yang J, Chen X, et al (2024) Long-Term airport network performance forecasting with linear diffusion graph networks. *IEEE Transactions on Intelligent Transportation Systems* 25(11):18264–18278
- Yan Z, Yang H, Li F, et al (2022) A deep learning approach for short-term airport traffic flow prediction. *Aerospace* 9(1)
- Yan Z, Yang H, Wu Y, et al (2023) A multi-view attention-based spatial-temporal network for airport arrival flow prediction. *Transportation Research Part E: Logistics and Transportation Review* 170:102997
- Yin Y, Zhang S, Zhang Y, et al (2025) Aircraft trajectory prediction in terminal airspace with intentions derived from local history. *Neurocomputing* 615:128843
- Zaheer M, Kottur S, Ravanbakhsh S, et al (2017) Deep sets. In: Advances in Neural Information Processing Systems
- Zeng A, Chen M, Zhang L, et al (2023) Are transformers effective for time series forecasting? In: Proceedings of the AAAI Conference on Artificial Intelligence, pp 11121–11128
- Zeng W, Chu X, Xu Z, et al (2022) Aircraft 4d trajectory prediction in civil aviation: A review. *Aerospace* 9(2):91

Zeng Y, Hu M, Chen H, et al (2024) Improved air traffic flow prediction in terminal areas using a multimodal spatial–temporal network for weather-aware (MST-WA) model. *Advanced Engineering Informatics* 62:102935

Zhang Y, Xu S, Zhang L, et al (2024) Short-term multi-step-ahead sector-based traffic flow prediction based on the attention-enhanced graph convolutional lstm network (AGC-LSTM). *Neural Comput Appl* 37(20):14869–14888

Zhang Z, Guo D, Zhou S, et al (2023) Flight trajectory prediction enabled by time-frequency wavelet transform. *Nature Communications* 14:5258

Zhou T, Ma Z, Wen Q, et al (2022) FEDformer: Frequency enhanced decomposed transformer for long-term series forecasting. In: *Proceedings of the 39th International Conference on Machine Learning (ICML)*, pp 27268–27286

## 7 Acknowledgements

This work was supported by the related foundations. B.W. sincerely thanks Xiaofeng Gao and Jingyuan Wang for their valuable insights and discussions on air traffic flow modeling.

## 8 Author contributions

B.W., A.L., F.H., and Y.Y. conceived and led the research project. B.W. proposed the research idea, contributed to the methodology design, and revised the manuscript. B.W., A.L., and J.Z. developed the framework, devised the neural architecture, implemented the model, and conducted the experimental studies. Y.H. contributed to the experimental evaluation and results discussion. P.H. and G.J. conducted data preprocessing, organized the dataset, and assisted with the experiments and result analysis.

All authors participated in the discussion of the results. B.W., A.L., and Y.Y. wrote the manuscript with input from all authors. F.H., Y.Y., and T.L. supervised and sponsored the study. B.W., A.L., F.H., and Y.Y. approved the submission and accepted responsibility for the overall integrity of the paper.

## **9 Competing interests**

The authors declare no competing interests.

## **10 Additional information**

Correspondence and requests for materials should be addressed to Feng Hong and Yanwei Yu.